Calculation of the two-body scattering *K*-matrix in configuration space by an adaptive spectral method

2009 J. Phys. A: Math. Theor. 42 015201

(http://iopscience.iop.org/1751-8121/42/1/015201)

IOP PUBLISHING JOURNAL OF PHYSICS A: MATHEMATICAL AND THEORETICAL

J. Phys. A: Math. Theor. **42** (2009) 015201 (17pp) doi:10.1088/1751-8113/42/1/015201

Calculation of the two-body scattering *K*-matrix in configuration space by an adaptive spectral method

George Rawitscher

Department of Physics, University of Connecticut, Storrs, CT 06268, USA

Received 8 September 2008, in final form 10 October 2008
Published 19 November 2008
Online at stacks.iop.org/JPhysA/42/015201

Abstract

A spectral integral method (IEM) for solving the two-body, one-variable Lippmann–Schwinger equation for the wavefunction in configuration space is generalized to the case of the two-variable scattering *K*-matrix. The main difficulty is that in this case the driving term of the integral equation is discontinuous. It is found that the desirable features of the IEM, such as the economy of mesh points for a given required accuracy, are carried over also to this case even though the result is also discontinuous. The main innovation is a judicious choice of the partitions in coordinate space, plus a new recursion relation forward and backward to the point of discontinuity. For a simple exponential potential an accuracy of 7 significant figures is achieved for the *K*-matrix, with the number *N* of Chebyshev support points in each partition equal to 17. For a potential with a large repulsive core, such as the potential between two He atoms, an accuracy of 7 significant figures requires that *N* is increased to 65 support points per partition.

PACS numbers: 02.30.Rz, 02.70.−c, 31.15.−p, 34.50.−s

(Some figures in this article are in colour only in the electronic version)

1. Introduction

It is most common to solve the Lippmann–Schwinger integral equation for the scattering wavefunction or the scattering *T*-matrix in momentum space [1, 2] because this space is most closely related to the ingoing and outgoing momenta of the scattering process. However, there are applications for which it is convenient to formulate the respective integral equation, in configuration space. One such application occurs if the solution of the three-body Faddeev integral equations is to be carried out in configuration space, since in this case the two-body scattering matrices for each of the three arrangements are required [3]. Another reason to explore methods to calculate the *T*-matrix in configuration space is that for the description of the scattering of atoms, not only a higher accuracy than for nuclear physics applications [4, 5]

is needed[1], but also, there can exist large repulsive cores and long-range tails in the interaction potential that cause difficulties in the momentum space representation.

Recently a method became available for solving the one-variable Lippmann–Schwinger integral equation in configuration space for the two-body scattering wavefunction [6–8], or for the bound state wavefunction [9]. The method is economical as well as accurate [10], and is based on the spectral expansion of the wavefunction into a set of Chebyshev polynomials, one expansion for each partition, together with a procedure of choosing the partitions in an adaptive manner. The T- or K-matrix is a function of two variables. It obeys a one-dimensional integral equation which is very similar to that for the wavefunction, which however has a discontinuity at a point where the two variables have the same value. It is the purpose of the present paper to show that it is possible to extend the IEM method to the calculation of the scattering matrix (the real K-matrix in this case), which is achieved by reconfiguring the partitions in such a way that the end of one partition is placed at the point of (the derivative) discontinuity of the driving term. This requires a new set of recursion relations for the coefficients that connect the K-wavefunction in one partition to that in the adjoining one, as will be described. Numerical tests performed for particular cases show that there is no loss of the spectral accuracy of approximately 7–8 significant figures. Integrals of K-matrices over arbitrary (but continuous) functions in configuration space lead to Lippmann–Schwinger integral equations with driving terms that are continuous, and the corresponding numerical procedure has already been described [11].

One difference between the treatments in configuration and momentum spaces is that the structure of the Green's function singularity is quite different. In configuration space the Green's function has a discontinuity in the derivative, while in momentum space it has a pole. Hence, configuration space solutions offer an independent and different approach from the momentum space solutions that can be useful for certain situations. The present study makes it possible to begin to compare the calculations in the two spaces. A section which illustrates some comparisons are included here. One example is the case of long-ranged potentials, such as the Coulomb potential, for which the configuration space is believed to be more economical. Another example is the case when the potential function has a large repulsive core, such as for the interaction between atoms. It is possible that in this case the momentum space treatment is more appropriate, depending on the nature of the repulsive core.

2. Theoretical considerations

Let us consider only one dimension described by the variable r which resides in configuration space, rather than in momentum space, and extends from 0 to ∞. The Schrödinger equation for the wavefunction $\psi(r)$ is

$$(\nabla + E)\psi(r) = V\psi(r) \tag{1}$$

where $\nabla = \mathrm{d}^2/\mathrm{d}r^2$ is the Laplacian, E is the energy, assumed positive here, and V is the 'local' potential, all in units of inverse length squared. The operator

$$(\nabla + E) = H_0 \tag{2}$$

is the 'free' Hamiltonian, the corresponding Green's function is denoted as $\mathcal{G}_0(E; r, r') = H_0^{-1}$, and the corresponding integral equation that solves equation (1) for ψ is

$$\psi(r) = \varphi(r) + \int_0^\infty \mathcal{G}_0(E; r, r')V(r')\psi(r')\,\mathrm{d}r'. \tag{3}$$

[1] According to Glöckle, private communication, the accuracy of three-body calculations in momentum space is between 3 and 4 significant figures, that is sufficient for nuclear physics applications.

Here $\varphi(r)$ is the 'undistorted' free on-shell wavefunction (usually a complex plane wave in three dimensions, but assumed real in this case), solution of $(\nabla + E)\varphi(r) = 0$, and is the 'driving term' of equation (3). For the case of zero angular momentum $\varphi(r) = \sin(k_T r)$, where $k_T = \sqrt{E}$ is the 'on-shell' wave number. The usual physical boundary conditions for positive energies are that

$$\psi(r \to 0) \to 0 \qquad \text{and} \qquad \psi(r \to \infty) \to N \sin(k_T r + \delta) \tag{4}$$

where N is an irrelevant normalization constant, and δ is the phase shift.

The K-matrix is a function of two (one-dimensional) variables, that has the following equivalent properties

(1)

$$\int_0^\infty K(E; r, r')\varphi(r')\,\mathrm{d}r' = V(r)\psi(r), \tag{5}$$

(2)

$$K(E; r, r') = V(r)\delta(r - r') + V(r)\int_0^\infty K(E; r, \bar{r})\mathcal{G}_0(E; \bar{r}, r')\,\mathrm{d}\bar{r}, \tag{6}$$

(3)

$$K(E; r, r') = V(r)\delta(r - r') + V(r)\mathcal{G}(E; r, r')V(r'). \tag{7}$$

In equation (7) $\mathcal{G}(E; r, r')$ is the 'distorted' Green's function $(\nabla - V + \mathrm{i}\varepsilon + E)^{-1}$. The derivation of equation (7) is based on several identities, such as

$$\psi = (1 - \mathcal{G}_0 V)^{-1}\varphi = (1 + \mathcal{G}V)\varphi, \tag{8}$$

where the integration signs have been left out. Another such relation is $T = (1 - V\mathcal{G}_0)^{-1}V$.

The effect of V on the phase shift δ is contained entirely in the K-matrix since, in view of equations (4) and (5), $\tan(\delta) = -(1/k_T)\int_0^\infty \mathrm{d}r \sin(k_T r)K(r, \bar{r})\sin(k_T \bar{r})\,\mathrm{d}\bar{r}$. Since V decreases to zero at large distances, K decreases in the same way as r and $\bar{r}$ tend to infinity, and hence the integral above need not be carried out to as large a distance as the solution of equations (1) or (3) for ψ. This point clarifies the computational advantage of solving for K rather than for ψ, but at the same time the short-range repulsive core is emphasized and needs a more careful numerical treatment.

An alternate form of writing equation (7) is

$$K(E; r, r') = V(r)\delta(r - r') + R(E; r, r'). \tag{9}$$

where R, in view of equation (6), obeys an integral equation with a discontinuous driving term $V(r)\mathcal{G}_0(E; r, r')V(r')$,

$$R(E; r, r') = V(r)\int_0^\infty \mathcal{G}_0(E; r, \bar{r})R(E; \bar{r}, r')\,\mathrm{d}\bar{r} + V(r)\mathcal{G}_0(E; r, r')V(r'), \tag{10}$$

which is the equation to be solved. Here $\mathcal{G}_0$ is the undistorted (free) two-body Green's function, that, for the partial wave in configuration space with angular momentum $L = 0$, is given by the well-known expression

$$\mathcal{G}_0(E; r, \bar{r}) = -\frac{1}{k_T}F(E; r_<)G(E; r_>), \tag{11}$$

where $F(E; r) = \sin(k_T r)$; $G(E; r) = \cos(k_T r)$, and where $r_<$ and $\mathrm{r}_>$ are respectively the lesser or the larger of r and $\bar{r}$.

In view of equation (7),

$$R = V(r)\mathcal{G}(E; r, r')V(r'), \tag{12}$$

however, this relation is not made use of here because (a) in the presence of large repulsive cores the regular and irregular solutions of equation (1), in terms of which $\mathcal{G}(E; r, r')$ can be constructed, present numerical accuracy difficulties (as is explained at the end of appendix B) and (b) integral equations of the type of equation (10), that have different discontinuous driving terms can be handled numerically by the methods described here. Nevertheless equation (12) is useful, because it shows that R is symmetric and discontinuous, properties that also follow from the nature of the driving term in equation (10). It also shows that R is semi-separable in its two variables, an important property in configuration space. One physical interpretation of $R(E; r, r')$ is that its integral over F represents all second- and higher-order Born terms of the iterative solution of the L–S equation (3) for the wavefunction. A relation between the K-matrix, the potential V, and the real part of the scattering wavefunction ψ, that will be used for numerical checking purposes, is equation (5) that, in the present notation is

$$V(r)\psi(r) = \int_0^\infty K(E; r, \bar{r})F(E; \bar{r})\,\mathrm{d}\bar{r}. \tag{13}$$

3. The spectral method

A very brief review of this method [6] is given below. The application to the solution of equation (10) is described in detail in [12], and a description of the solution of the Lippmann–Schwinger equation with a continuous general driving term, different from that in equation (3), is given in [11]. One essential feature of the IEM is to divide the entire radial range into partitions, and expand the unknown function in each partition in terms of a small number N ($\simeq$17) of basis functions such as Chebyshev or Legendre polynomials. Partitioning has the merit (a) that the number of mesh points is very economical, since the partitions are concentrated automatically and adaptively in those regions where the function varies most rapidly, (b) the accuracy control of the spectral expansions is also maintained and (c) the singularity in the driving term of equation (10) described below, can be easily handled by placing the boundary between two partitions at the position of the singularity. The basic reason that the same partitioning procedure can still be maintained is that the integral in equation (10) is over one variable only, i.e., the second variable is introduced only parametrically through the driving term

$$\mathfrak{D}(r, r') = V(r)\mathcal{G}_0(E; r, r')V(r'). \tag{14}$$

For simplicity the energy variable is suppressed in what follows, and the angular momentum quantum number is assumed to be $\ell = 0$. In order to simplify the notation, it is useful to define the functions $\mathfrak{F}$ and $\mathfrak{G}$ as

$$\mathfrak{F}(r) = F(r)V(r) \tag{15}$$

$$\mathfrak{G}(r) = G(r)V(r) \tag{16}$$

in terms of which the driving term, equation (14), is given by

$$\mathfrak{D}(E; r, r') = -\frac{1}{k_T}\mathfrak{F}(E; r_<)\mathfrak{G}(E; r_>), \tag{17}$$

where $r_< = r$ and $r_> = r'$ if $r < r'$, or the reverse if $r > r'$. Initially, without regard of the position of r', the radial interval is truncated at an upper limit $0 \leqslant r \leqslant r_{\max}$, and that region is divided into M partitions. The size of each partition and the corresponding number M is determined automatically by the accuracy criterion according to the properties of Chebyshev expansions [7, 8], and for this reason these partitions are denoted as Chebyshev partitions in

what follows. The lower and upper limits of each partition $i = 1, 2, \ldots, M$ are denoted by t_{i-1} and t_i, respectively,

$$t_{i-1} \leqslant r_i < t_i, \tag{18}$$

and if r is contained in partition i it is denoted as r_i. A second mesh of N_{rp} equidistant points r' is set up in the same radial interval $[0, r_{\max}]$ at a fixed mesh distance of h_{rp}. For a point r' on this mesh that falls into a particular Chebyshev partition j, this partition is further divided into two, with r' located at the border between the two sub-partitions. The left (right) sub-partition is denoted as $j_L(j_R)$.

The integral operator $\mathcal{G}_0$ restricted to partition i is denoted as $\mathcal{G}_i$ and when applied to a function $\xi(\bar{r})$ the result is

$$\mathcal{G}_i\xi \equiv -\frac{1}{k_T}G(r_i)\int_{t_{i-1}}^{t_i} F(\bar{r})\xi(\bar{r})\,\mathrm{d}\bar{r} - \frac{1}{k_T}F(r_i)\int_{r_i}^{t_i} G(\bar{r})\xi(\bar{r})\,\mathrm{d}\bar{r}. \tag{19}$$

Inserting equation (9) into (10) one obtains

$$R_{i,j} - V(r_i)\mathcal{G}_i R_{i,j} = \mathfrak{D}(r_i, r'_j) + \mathfrak{G}(r_i)\int_0^{t_{i-1}} (-)\frac{1}{k_T}F_0(\bar{r})R(\bar{r}, r'_j)\,\mathrm{d}\bar{r}$$
$$+ \mathfrak{F}(r_i)\int_{t_i}^{r_{\max}} (-)\frac{1}{k_T}G_0(\bar{r})R(\bar{r}, r'_j)\,\mathrm{d}\bar{r}. \tag{20}$$

where the left-hand side of equation (20) denotes $R(r_i, r'_j) - V(r_i)\int_{t_{i-1}}^{t_i}\mathcal{G}_0(r, \bar{r})R(\bar{r}, r')\,\mathrm{d}\bar{r}$. The integrals in equation (20) do not depend on r_i, and are denoted as

$$A_i(r'_j) = -\frac{1}{k_T}\int_{t_i}^{r_{\max}} G(\bar{r})R(\bar{r}, r'_j)\,\mathrm{d}\bar{r} \tag{21}$$

$$B_i(r'_j) = -\frac{1}{k_T}\int_0^{t_{i-1}} F(\bar{r})R(\bar{r}, r'_j)\,\mathrm{d}\bar{r}. \tag{22}$$

In view of the linearity of the operator $(1 - V\mathcal{G}_i)$ on the left-hand side of equation (20), the solution of equation (20) can be written as [6] a linear combination of three functions Y, Z and S

$$R(r_i, r'_j) = A_i(r'_j)Y_i(r_i) + B_i(r'_j)Z_i(r_i) + S_{i,j}(r_i, r'_j) \tag{23}$$

that respectively are the solutions of

$$[1 - V(r_i)\mathcal{G}_i]Y_i = \mathfrak{F}(r_i) \tag{24}$$

$$[1 - V(r_i)\mathcal{G}_i]Z_i = \mathfrak{G}(r_i) \tag{25}$$

$$[1 - V(r_i)\mathcal{G}_i]S_{ij} = \mathfrak{D}(r_i, r'_j) \tag{26}$$

in each interval i. The solutions Y and Z are obtained by expanding them into Chebyshev polynomials and calculating the coefficients of the expansion by the Curtis–Clenshaw method [13]. A new feature is the appearance of the third function S_{ij}, that, in view of equation (17) is given by

$$S_{ij}(r_i, r'_j) = -\frac{1}{k_T}Y_i(r_i)\mathfrak{G}(r'_j) \qquad i < j \tag{27}$$

$$S_{ij}(r_i, r'_j) = -\frac{1}{k_T}Z_i(r_i)\mathfrak{F}(r'_j) \qquad i > j. \tag{28}$$

The calculations of the coefficients A and B is achieved by means of recursion relations, described in [11]. They consist in propagating the coefficients forward from partition $i = 1$ to partition j_L, and backward, from partition M to j_L. By equating the two results in partition j_L, all the coefficients can be determined as a function of r'. These forward and backward propagations to the point r'_j bear some similarity to the method described in [9] for the calculation of energy eigenvalues of the Schrödinger equation, where the wavefunction is also propagated forward and backward to an internal matching point. For $i \neq j$ the result is a semi-separable expression of the form

$$R(r_i, r'_j) = [A_i(r'_j) - \mathfrak{G}(r'_j)/k]Y_i(r_i) + B_i(r'_j)Z_i(r_i), \qquad i < j \tag{29}$$

$$R(r_i, r'_j) = A_i(r'_j)Y_i(r_i) + [B_i(r'_j) - \mathfrak{F}(r'_j)/k]Z_i(r_i), \qquad i > j. \tag{30}$$

This semi-separability leads to an economy of the computational effort, and is in agreement with the semi-separable nature of the distorted Green's function in equation (12).

If the driving term in equation (17) were set to zero, the quantities $S_{i,j}$ in equation (26) would vanish, and hence equation (10) would be of the form

$$R(E; r, r') = V(r) \int_0^\infty \mathcal{G}_0(E; r, \bar{r}) R(E; \bar{r}, r')\, \mathrm{d}\bar{r}. \tag{31}$$

The solution R of this equation vanishes, unless the determinant of the discretized form of the operator $1 - V(r)\int_0^\infty \mathrm{d}\bar{r}\, \mathcal{G}_0(E; r, \bar{r})$ is zero. This determinant does vanish for particular discrete energies which are the bound states of the two-body system. As the energy E ranges over the negative values which include bound state energies, poles in the R-matrix occur. However, the exploration of these singularities will be left to a future study.

4. Numerical examples

Two different potentials in equations (1) or (10) are used for the numerical examples presented here. One is a simple exponential potential and the other is a potential describing the interaction between two helium atoms, based on the potential TTY [14, 15][2]. For the He–He case a repulsive core is applied for a distance less than $r_{\mathrm{cut}} = 4.5a_0$. This core is of the form $a + br + cr^2$, with the coefficients a, b and c determined such that the repulsive core is equal to the value, the first, and second derivatives of TTY at $r = r_{\mathrm{cut}}$. Graphs of the He–He potential, and the corresponding repulsive cores, are shown in figures 3 and 4, respectively, in [11]. The numerical IEM calculations are carried out from $r = 0$ to $r = r_{\max}$, so as to include the effect of the core accurately, in contrast to setting to zero the wavefunction in the radial region from the origin to a particular core radius. In [11] it was shown that the repulsive core had no significant effect for values of $r_{\mathrm{cut}} < 3a_0$. The value of the accuracy parameter is $\mathrm{tol} = 10^{-8}$, and the wave number is $k_T = 1.5a_0^{-1}$. The potential and the wave number are in units of inverse length squared and inverse length, respectively. The length units are either fm for the exponential case, or Bohr a_0 for the atomic case, as is described in the appendix.

4.1. The exponential example

The potential in equation (10) is $V(r) = \pm\exp(-ar)$, with $a = 1\,\mathrm{fm}^{-1}$. The R-matrix for the repulsive case (+sign) is shown in figure 1, and the behavior of the diagonal part of R is shown in figure 2. The derivative discontinuity of $R(r, r')$ at $r = r'$ is clearly visible in figure 1, and

[2] The authors thank Professor F A Gianturco of [15] from the University of Rome 'La Sapienza' for stimulating conversations and for permission to use his TTY Fortran code.

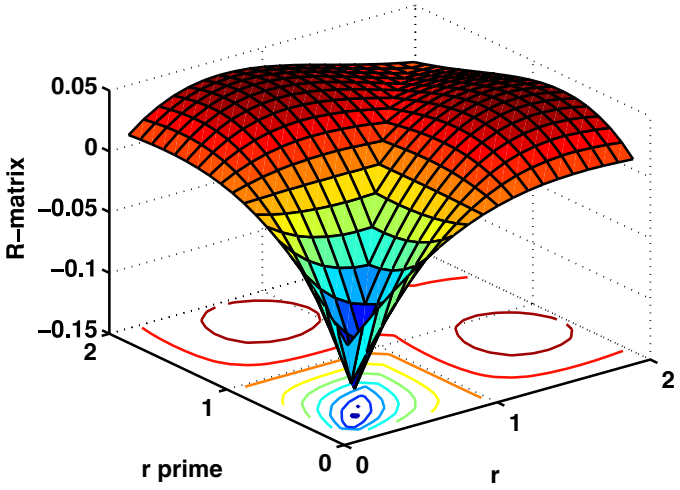

Figure 1. The R-matrix for the repulsive exponential potential $V = \exp(-ar)$. The wave number k_T is 1.5 fm^{-1}, $a = 1$ fm^{-1} and R is in units of fm^{-3}. The discontinuity in the derivative, for $r = r'$ is clearly visible.

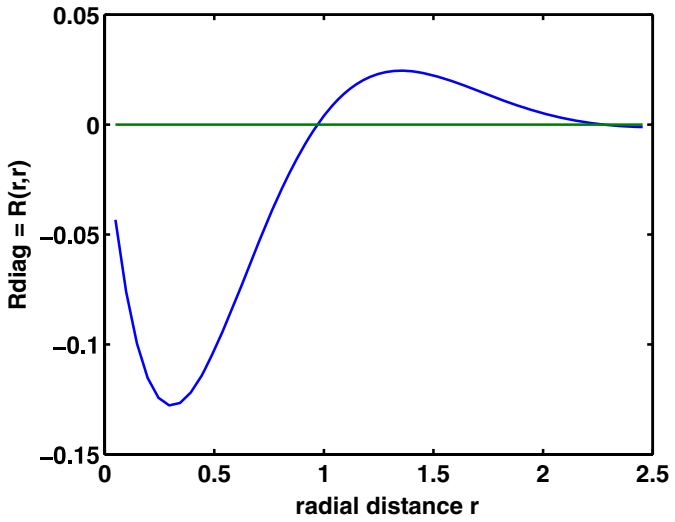

Figure 2. The diagonal part of the R-matrix, shown in figure 1.

it is also seen that R is large in the radial region where the potential is large, in agreement with equation (12). These features are also present for the He–He case, described below.

4.2. The He–He case

For the He–He case the potential is shown in figure 3. It has a strong repulsive core, that is not adequately represented by the formula described in [14, 15] (see footnote 2). Since the result for the R-matrix depends significantly on the nature of the repulsive core, an 'artificial'

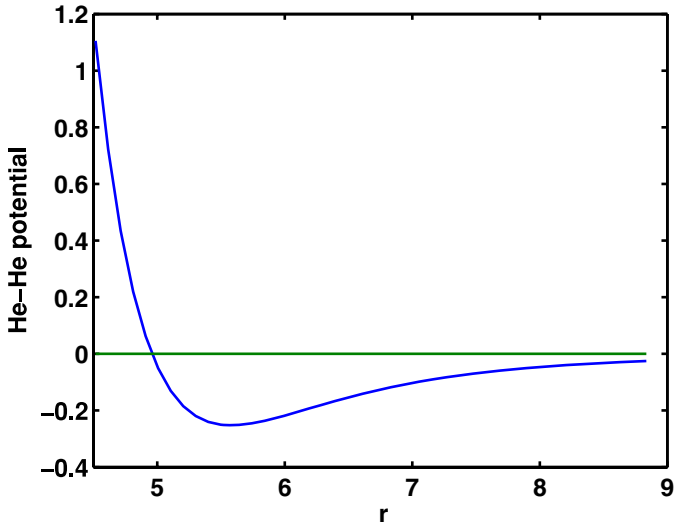

Figure 3. The He–He atom interaction, based on the potential TTY [14]. The units for the distance are a_0 (the Bohr radius) and $(a_0)^{-2}$ for the potential. For distances less than $4.5a_0$ (not shown here) a repulsive soft core is matched to this potential, as described in the text. At $r \simeq 0$ its value is $\simeq 150(a_0)^{-2}$. The He–He dimer is very weakly bound, with a binding energy of $3.02 \times 10^{-5}(a_0)^{-2}$, or $\simeq 10^{-7}$ eV. Upon division by the factor 7296.3 this potential is transformed to atomic energy units, as described in [9].

repulsive soft core was used to replace the repulsive core of TTY for distances $0 < r \leqslant r_{\rm cut}$. This core is of the form $a + br + cr^2$, with the coefficients a, b and c determined such that the repulsive core is equal to the value, the first, and second derivatives of TTY at $r = r_{\rm cut}$. This form of the core is less unphysical than the 'cut-off' core used in our previous numerical calculations of the binding energy of the He–He dimer [9], for which V was replaced by a constant value $V(r_{\rm cut})$ for $0 < r \leqslant r_{\rm cut}$.

The R-matrix at small distances is shown in figure 4. The values of R are very large in the region or the large repulsive core, but they become smaller at larger distances for which the potential becomes progressively smaller, as is illustrated in figures 5 and 6.

The diagonal parts of the He–He R-matrix are shown in figures 7 and 8, for small and large distances, respectively.

5. Comparison between the momentum and configuration space representations

In this section the momentum space representations of the K-matrix will be compared with a hybrid representations for the interaction between two He atoms. In the hybrid representation one coordinate is in configuration space and the other in momentum space, while in the momentum representation both coordinates are in momentum space. The two representations are defined by the integrals

$$\langle r|T|k_d\rangle = \int_0^{r\,\max} T(r, r')\sin(k_d r')\,{\rm d}r', \tag{32}$$

where the integral (32) is evaluated numerically according to [11], and

$$\langle k|T|k_d\rangle = \int_0^{r\,\max} \langle r|T|k_d\rangle \sin(kr)\,{\rm d}r. \tag{33}$$

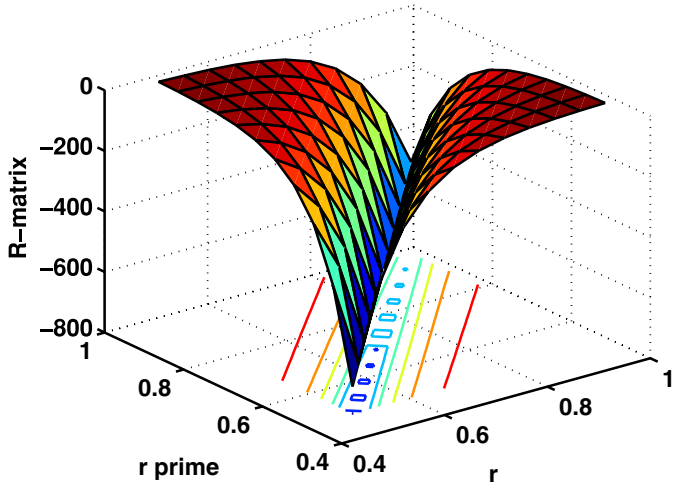

Figure 4. The R-matrix for the He–He potential at distances well inside of the repulsive core, with $r_{\rm cut} = 4.5a_0$, and $k_T = 1.5a_0^{-1}$. The units of R are a_0^{-3}.

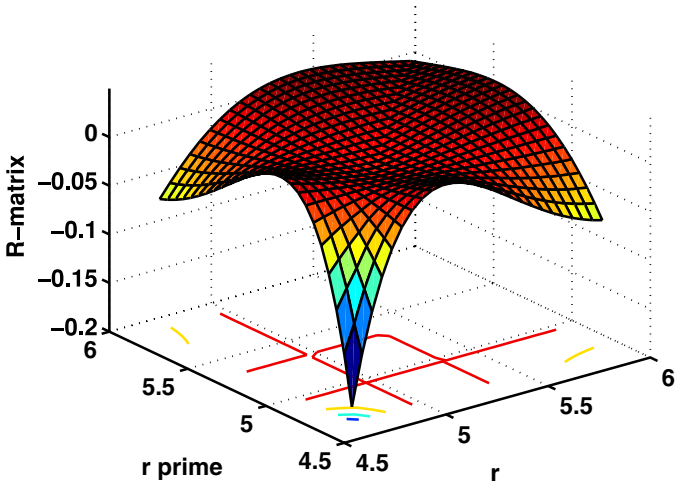

Figure 5. The He–He R-matrix, same as in figure 4, but at larger distances, straddling the end of the repulsive core and the attractive potential valley.

The He–He potential described above was used with two different repulsive cores: a mild repulsive core defined by $r_{\rm cut} = 4.5a_0^{-1}$ and a strong repulsive core defined by $r_{\rm cut} = 3.5a_0^{-1}$. These repulsive cores are softer and more rounded than the repulsive cores described in section 4 above, so as not to introduce excessive momentum components into the momentum representation of K. They are obtained by means of a combination of exponential functions of r, and are 'grafted on' to the He–He potential so that the value and derivative of the repulsive core agree with the corresponding values of the He–He potential at $r = r_{\rm cut}$. Figure 9 illustrates these properties. For $r_{\rm cut} = 3.5a_0$ the potential reaches a maximum value of $472a_0^{-2}$ at $r = 0$. The results for the two representations of K are shown in figures 10 and 11, respectively.

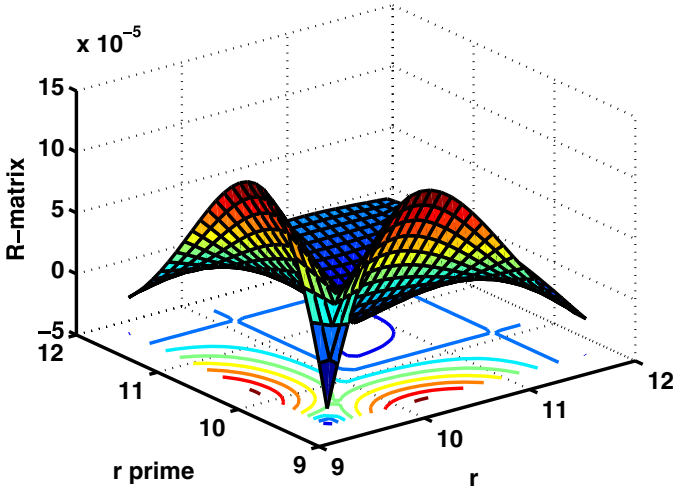

Figure 6. The He–He R-matrix, same as in figure 4, at distances between 9 and $12a_0$ where the potential is of the r^{-6} form. The value of R is of the order of 10^{-5} $(a_0)^{-3}$.

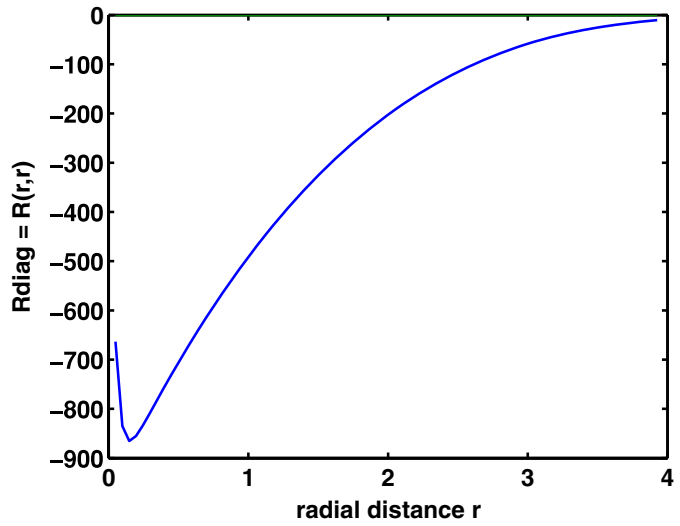

Figure 7. The diagonal part of the He–He R-matrix, shown in figure 4 at small distances.

While in the hybrid representation (top panels of both figures) both types of repulsive cores give a result that is not strongly oscillatory at large distances, the momentum representation remains oscillatory out to larger distances in the momentum variable k. This is particularly clear for the case for $r_{\rm cut} = 3.5a_0$ and $k_d = 4.5\ a_0^{-1}$. The figures also show that in momentum space the weak repulsive core is easier to handle than the stronger repulsive core, in that the oscillations at large momenta have a smaller amplitude.

A similar result was found for the case of a nucleon–nucleon potential (called Malfliet–Tjon in nuclear physics applications) composed of two exponential functions of different

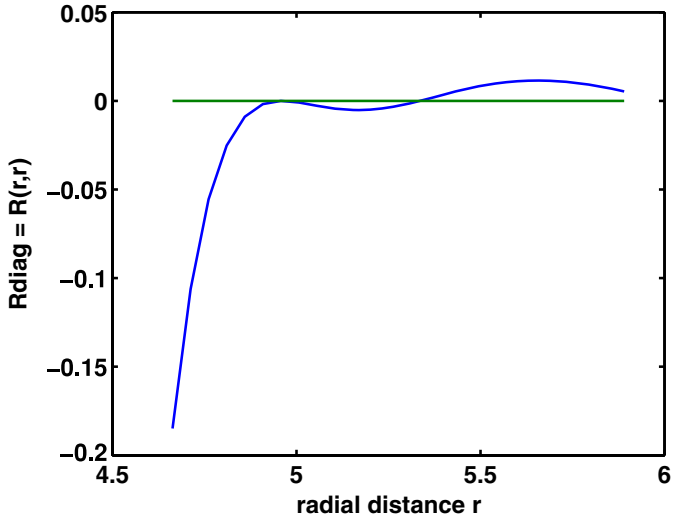

Figure 8. Same as figure 7 for large distances.

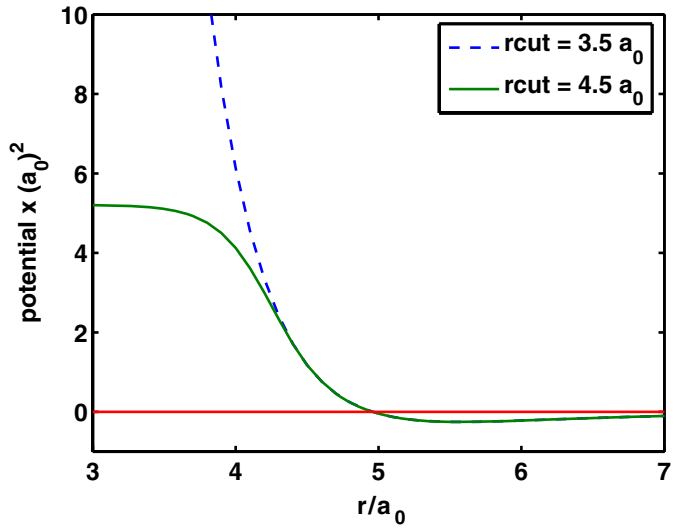

Figure 9. Two repulsive potential cores grafted on to the He–He TTY potential at the distances $r_{\rm cut}$, used for the comparison of the configuration and momentum space representations of the K-matrix. These repulsive cores are softer than those displayed in figure 3.

ranges. At short distances the potential is repulsive, reaches a negative minimum as r increases, and finally decays exponentially to zero at large distances. In the momentum representation the K-matrix decreases to zero in the momentum variable much more slowly than in the r-variable in the hybrid representation. Furthermore, when a repulsive Coulomb potential is added the K-matrix, the momentum representation is much more sensitive to the presence of the Coulomb potential than the hybrid representation.

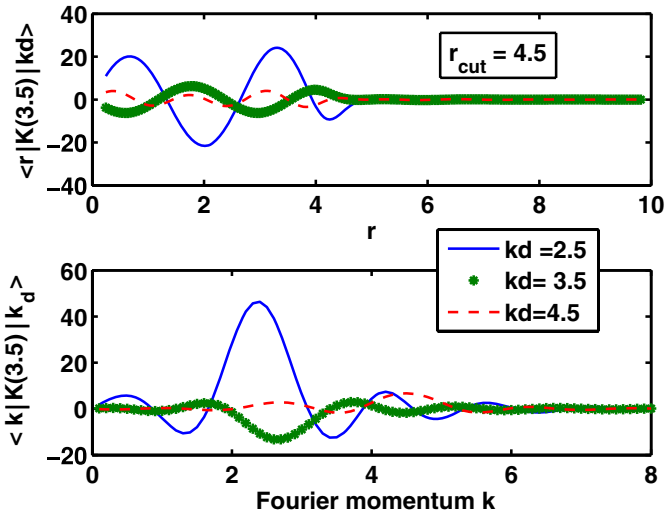

Figure 10. Comparison of the hybrid and the full momentum representations (upper and lower panels, respectively) of the K-matrix for the He–He potential with a soft repulsive core illustrated in figure 9 for $r_{\rm cut} = 4.5a_0$. The momentum k_T that defines the energy of the K-matrix is $3.5a_0^{-1}$. The momenta k and k_d are in units of a_0^{-1}, and the units of $\langle r|K|k_d\rangle$ and $\langle k|K|k_d\rangle$ are a_0^{-2} and a_0^{-1}, respectively.

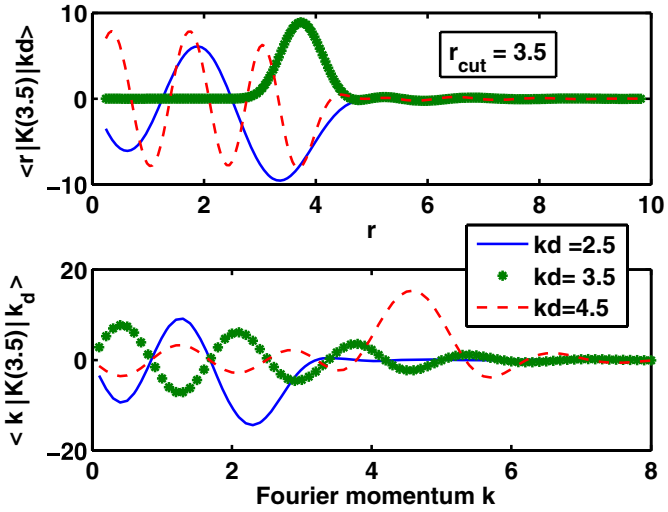

Figure 11. Same as figure 10 for a more repulsive soft core, described by $r_{\rm cut} = 3.5a_0$.

6. Summary and conclusions

In this paper the spectral IEM method for solving the one-variable Lippmann–Schwinger integral equation (L–S) in configuration space for the wavefunction [6, 8], or for obtaining integrals of the two-body scattering K-matrix over another function [11], is extended to the solution of a two variable L–S equation, also in configuration space. The numerical focus is for the calculation of a function $R(r, r')$ which arises when one subtracts from the K-matrix a

delta-function multiplying the (local) potential, equation (9). The L–S equation for the latter, equation (10), is of the type addressed in the present numerical calculation. The driving term for this equation is continuous but has a discontinuous derivative at $r = r'$. That discontinuity also propagates into the R-matrix, and makes the calculation more cumbersome. This difficulty is overcome by constructing the partitions into which the radial domain is divided in such a way that the point r' is located at the end-point of a partition without affecting the other partitions. This procedure is repeated for all values of r' contained in a prescribed set of mesh of points. Otherwise the calculation is very similar to the spectral IEM procedure for the solution of the one-variable L–S equation, whose accuracy and reliability was previously demonstrated in various applications [9, 10]. The accuracy of the K-matrix attained in this procedure, of between 7 or 8 significant figures, is demonstrated by verifying the accuracy and validity of an identity, equation (13), as documented in appendix B. Appendix C documents the stability and accuracy of the IEM for obtaining bound-state energies, and compares the result for the He–He dimer with that of [16].

Two numerical examples are described. One, in which the potential is a simple exponential function of r, and the other in which the potential describes the interaction between two helium atoms [14]. The latter example was chosen because of the presence of a strong repulsive core at small interatomic distances, and hence is suitable to test how well the method could handle the repulsive core. For the exponential case the number N of Chebyshev support points in each partition could remain at the 'canonical' value of 17, but for the He–He case, in view of the presence of the strong repulsive core, the number of support points in each partition had to be increased to 65. With that change no difficulty was found in treating the repulsive core. A preliminary comparison of the configuration and momentum representations of the K-matrix shows that in the configuration space the representation is contained in a relatively small radial interval, small compared to the radial extent of the scattering wavefunction, while in momentum space the momentum interval is much larger. This result needs to be studied in more detail, but is related to the fact that in configuration space the K-matrix is connected to the product of a wavefunction times the potential, as shown by equation (12). This is also why the repulsive core plays a larger role in the calculation of the K- (or) T-matrix than in the calculation of a wavefunction.

The main result of the present study is to show that the adaptive spectral integral equation method is well suited to calculate the K- (or) T-matrix in configuration space. This, together with the ability of the IEM to calculate integrals of the K-matrix over functions, all in configuration space [11], makes it now possible to return to configuration space for the calculation of scattering functions defined through integral equations, including the solution of the three-body Faddeev integral equations in configuration space.

Acknowledgments

The author is greatly indebted to Professor Walter Glöckle for stimulating and consistent help with this work, and for pointing out its underlying importance with regards to the envisaged three-body calculations. The author is also grateful to Professor I Koltracht at the University of Connecticut (recently deceased), for help with the computational–mathematical aspects of this work.

Appendix A. Units and dimensions

The potential energy $\bar{V}$ and the energy $\bar{E}$ in the Schrödinger equation are normally given in units of energy, while the distance is in units of length (ℓ). By multiplying all terms in the

Schrödinger equation by $2\mu/\hbar^2$, where μ is the reduced mass of the two colliding particles, and $\hbar$ is Planck's constant divided by 2π, then all terms in the scaled Schrödinger equation acquire dimensions of ℓ^{-2}. The new potential energy V and the energy E then are

$$V = Q\bar{V}, \tag{A.1}$$

$$E = k^2 = Q\bar{E}, \tag{A.2}$$

where Q is a scaling factor.

For nuclear physics applications $\bar{E}$ and $\bar{V}$ are given in MeV, the radial distance in fm and the corresponding value of Q is

$$Q_N = 2\mu/\hbar^2. \tag{A.3}$$

The corresponding scaled Schrödinger equation is equation (1), and the corresponding L–S equation is (3). The dimension of the Green's function $\mathcal{G}_0$, equation (11), is ℓ^1 (for the nuclear case $\ell \equiv fm$) and hence the operator $\mathcal{G}_0(r, r')V(r')\,dr'$ has no dimension. In view of equation (13), and since F and ψ have no dimension, the T- or K-matrix has dimension ℓ^{-3}. This dimension is compatible with equation (9), since the delta function has dimension ℓ^{-1}. The dimension of R is also ℓ^{-3}, which is compatible with equation (10). The dimension of A and B, equations (21) and (22), is ℓ^{-1}, the dimension of Y and Z, equations (24) and (25), is ℓ^{-2}, and that of S, (26) is ℓ^{-3}. The quantities $\mathfrak{G}$ or $\mathfrak{F}$ have dimensions ℓ^{-2}, and hence equations (29) and (30) are dimensionally self-consistent, each term having the dimension ℓ^{-3}.

For atomic physics applications $\bar{E}$ is given in atomic energy units $2\mathbb{R}$, ($\mathbb{R} \simeq 13.606\,\mathrm{eV}$) and the distance r in units of the Bohr radius a_0, in which case

$$Q_A = \frac{2\mu}{\hbar^2}a_0^2 \times 2\mathbb{R} = \frac{2\mu}{m_e}, \tag{A.4}$$

where m_e is the mass of the electron.

Appendix B. Accuracy tests

The accuracy of the functions Y and Z in each partition, equations (24) and (25), determined by the size of the partitions, is better than $\mathrm{tol} = 10^{-8}$. In order to obtain a measure of the loss of accuracy that takes place in the subsequent steps of the calculation, the following two tests are performed: one that checks the symmetry of the R-matrix, and the other that performs the numerical integral

$$\mathfrak{I}_R(\mathfrak{r}') = \int_0^{r_{\max}} R(r, r') \times F_0(r)\,dr \tag{B.1}$$

which, according to equation (13), should be equal to

$$\mathfrak{I}_L(r') = [\psi(r') - F_0(r')]V(r'). \tag{B.2}$$

In table B1 the values of $\mathfrak{I}_L$ and $\mathfrak{I}_R$ above are compared in order to check the accuracy of their agreement with each other. The accuracy of $\mathfrak{I}(r')$ defined in equation (B.2) is better than 8 significant figures as was previously demonstrated in various applications [9, 10]. For the

Table B1. L and R are the values of equations (B.2) and (B.1), respectively. The numbers after the e indicate the powers of ten by which the numbers are to be multiplied.

n	$r = \frac{n\times\pi}{16}$		Exp. pot$'l$	$He - He$pot$'l$
10	$\simeq$1.96	L	**3.854 316 05**(e − 2)	**−1.079 593 140**(e1)
		R	3.854 316 05(e − 2)	−1.079 593 140(e1)
15	$\simeq$2.95	L	**4.052 449** 38(e − 3)	**2.348 628 29**(e1)
		R	4.052 449 31(e − 3)	2.348 628 33(e1)
20	$\simeq$3.93	L	**−5.633 010** 764(e − 3)	**4.121 564 23**
		R	−5.633 010 723(e − 3)	4.121 564 14
25	$\simeq$4.91	L	**−1.073 578 0**42(e − 3)	**1.414 453 3**(e − 2)
		R	−1.073 578 029(e − 3)	1.414 4530(e − 2)
30	$\simeq$5.89	L	**7.192 930** 11(e − 4)	**8.245 9426**(e − 2)
		R	7.192 930 28(e − 4)	8.245 9429(e − 2)
35	$\simeq$6.87	L	**2.055 220 6**7(e − 4)	**3.800** 324 58(e − 2)
		R	2.055 220 71(e − 4)	3.800 323 95(e − 2)
40	$\simeq$7.85	L	**−8.596 136** 54(e − 5)	**1.935 6054**(e − 2)
		R	−8.596 136 75(e − 5)	1.935 6055(e − 2)

exponential case the number of Chebyshev support points in each partition is $N = 17$, and only four partitions are required to cover the interval from $r = 0$ to $r = 25$.

For He–He case, if $N = 17$, the interval from 0 to 250 requires 26 partitions, 11 of which lie in the region of the repulsive core. The corresponding accuracy of the integral $\mathfrak{I}(r)$ (not displayed in the table) is three to four significant figures. As N is increased, the size of each partition increases, correspondingly the number of partitions decreases. The accuracy of R increases the smaller the number of partitions, because the Chebyshev support points are those that carry the large change in the R-values, rather than the coefficients A and B. The results for $\mathfrak{I}(r)$ for $N = 65$ are shown in 'L' lines of table B1, from which one can deduce an accuracy for R of at least 7 significant figures. For this case there are only four partitions in the region $[0 \longrightarrow 5]$ of the repulsive core, and four more partitions that cover the whole remaining distance $[5 \longrightarrow 250]$. These accuracy results for both the exponential and the He–He cases are confirmed by the degree of symmetry obtained for the R-matrix.

Using MATLAB, version 7.0.1.24704(R14) on a 2.8 GHz intel computer, the total time required for a He–He calculation of $R(r, r')$, with $n = 1273$ equidistant meshpoints for each r and r', $r_{\max} = 250$, $N = 17$ and tol $= 10^{-8}$ requires 114 s. (This time scales like n^2.) For the same calculation, but with $N = 65$, the total MATLAB time is 261 s. The corresponding calculation of the wavefunction ψ, for $r_{\max} = 1500$ and also 1273 equidistant meshpoints takes between 1 and 2 s.

The regular and irregular functions ψ and χ that make up the distorted Green's function, in terms of which the T- or K-matrix can be expressed, increase and decrease very rapidly, respectively, in the region of the repulsive core, making it difficult to assess their accuracy. For the He–He case, for $k = 1.5a_0^{-1}$, $V\psi$ increases by 11 orders of magnitude in the radial interval from $0.1 < r < 2a_0$, while $V\chi$ decreases by 12 orders of magnitude in the same interval. By contrast, the value of R changes approximately by only 3 orders of magnitude (see figure 7 in the main text) making the solution of the L–S equation for R numerically more reliable than the calculation of the distorted Green's function in the presence of a strong repulsive core.

Table C1. Comparison of the He–He binding energies obtained by various authors.

	B.E. (mK)	$\langle r \rangle$(nm)
[9], IEM	**1.314 61**	**5.1607**
[16], Dubna group	**1.309 62**	
[14], TTY	**1.316**	
Experiment (Grisenti)	**0.9–1.4**	$\mathbf{5.2 \pm 0.4}$

Table C2. Sensitivity of the He–He binding energy to the value of the cut-off radius $R_{\rm cut}$.

$R_{\rm cut}(a_0)$	B.E. (mK)	$\langle r \rangle(a_0)$
2.0	**1.314 6101**	**97.7419**
2.5	**1.314 6101**	**97.7419**
3.0	**1.314 6143**	**97.7418**
3.5	**1.321 9315**	**97.4935**

Appendix C. Accuracy of the He–He di-atom binding energy

The comparison of the result for the binding energy, obtained with an iterative spectral IEM method [9], with the most precise result of the Dubna group [16] was already presented in [9]. The comparison is reproduced below as table C1. In an e-mail exchange with the Dubna group asking what might have caused the discrepancy, Ms Kolganova suggested that the difference might have been due to a difference in the parametrization of the TTY potential.

In [10] we also studied the sensitivity of the binding energy to $r_{\rm cut}$. Again we find that for $r_{\rm cut} \leqslant 3.0a_0$ the results are insensitive to the value of $r_{\rm cut}$. The table from [10] is reproduced below as table C2. However the cut-off procedures in [10] and that in the present paper are not the same. In [10] the potential for $r \leqslant r_{\rm cut}$ is replaced abruptly by $V(r_{\rm cut})$, while in the present paper the change of V is more gradual.

References

[1] Landau R H *Quantum Mechanics II, A Second Course in Quantum Theory* (New York: Wiley) (chapter 6)

[2] Juliá-Díaz B, Lee T-S H, Matsuyama A and Sato T 2007 *Phys. Rev.* C **76** 065201
Matsuyama A, Sato T and Lee T-S H 2007 *Phys. Rep.* **439** 193–253

[3] Gloeckle W and Rawitscher G 2005 Three-atom scattering via the Faddeev scheme in configuration space arXiv:physics/0512010
Gloeckle W and Rawitscher G 2007 Scheme for an accurate solution of Faddeev integral equations in configuration space *Proc. of 18th Int. IUPAP Conf. on Few Body Problems in Physics Nucl. Phys.* A **790** 280–3

[4] Glöckle W, Witala H, Hüber D, Kamada H and Golak J 1996 *Phys. Rep.* **274** 107

[5] Golak J, Skibinski R, Witala H, Glöckle W, Nogga A and Kamada H 2005 *Phys. Rep.* **415** 89

[6] Gonzales R A, Eisert J, Koltracht I, Neumann M and Rawitscher G 1997 *J. Comput. Phys.* **134** 134–49
Gonzales R A, Kang S-Y, Koltracht I and Rawitscher G 1999 *J. Comput. Phys.* **153** 160–202

[7] Deloff A 2007 Semi-spectral Chebyshev method in quantum machanics *Ann. Phys.* **322** 1373

[8] Rawitscher G and Koltracht I 2005 An efficient numerical spectral method for solving the Schrödinger equation *Comput. Sci. Eng.* **7** 58

[9] Rawitscher G and Koltracht I 2006 An economical method to calculate eigenvalues of the Schrödinger equation *Eur. J. Phys.* **27** 1179–92

[10] Rawitscher G H *et al* 1999 Comparison of numerical methods for the calculation of cold atom collisions *J. Chem. Phys.* **111** 10418

Rawitscher G H, Kang S-Y and Koltracht I 2003 A novel method for the solution of the Schrodinger equation in the presence of exchange terms *J. Chem. Phys.* **118** 9149
[11] Rawitscher G and Gloeckle W 2008 *Phys. Rev.* A **77** 012707
[12] Rawitscher G 2007 arXiv:0711.4763
[13] Clenshaw C W and Curtis A R 1960 A method for numerical integration on an automatic computer *Numer. Math.* **2** 197
[14] Tang K T, Toennies J P and Yiu C L 1995 *Phys. Rev. Lett.* **74** 1546 (and private communication from K T Tang)
[15] Gianturco F A *TTY Fortran code* University of Rome
[16] Kolganova E A, Motovilov A K and Sandhas W A 2004 Scattering length of the helium-atom–helium-dimer collision *Phys. Rev.* A **70** 052711